Hybrid DCNN-Enabled Depolarizing Chipless RFID: Improving Tag Detection Across Varying Lossy Surfaces and Shapes

Nadeem Rather, *Member, IEEE*, Roy B. V. B. Simorangkir, *Member, IEEE*, Dinesh R. Gawade, *Graduate Student Member, IEEE*, John L. Buckley, *Member, IEEE*, Brendan O'Flynn, *Senior Member, IEEE*, and Salvatore Tedesco, *Member, IEEE*

Abstract*—This paper presents a comprehensive design and implementation approach for robust detection of depolarizing chipless RFID (CRFID) tags. Depolarizing tags are advantageous compared to co-polar CRFID tags due to their improved performance on RF-lossy materials. This work introduces the application of deep learning (DL) regression modelling to a specialised dataset of depolarised Radar Cross Section (RCS) measurements of a custom 3-bit CRFID tag, acquired through an extensive robot-based data acquisition method. A dataset of 12,600 depolarised Electromagnetic (EM) RCS signatures were collected using an automated data acquisition system to train and validate a 1-dimensional Convolutional Neural Network (1D CNN) architecture. A novel hybrid 1D CNN with Bi-LSTM and attention mechanism architecture was also implemented to visualize the model attention and improve detection performance. We present, for the first time reported in literature, a comprehensive design and AI implementation approach for reliably detecting identification (ID) information from depolarized signals. Also, we report the first instance of describing the impact of surface permittivity variations, tag deformations, tilt angles, and read ranges, all integrated into model training for enhanced robustness in detecting ID information. The developed models facilitate real-time identification and recording of objects, enhancing IoT applications in varied environments. It was observed that both models were able to generalize well to given data, with Model-1 achieving a low RMSE of 0.040 (0.66%) on an unseen test dataset. However, the hybrid model reduced the error further by 27.5% with a test RMSE of 0.029 (0.48%).

***Index Terms*—Chipless RFID, CNNs, deep learning, data acquisition, electromagnetic systems, machine learning, RCS, radio frequency, RFID, robot.**

Received 18 June 2025; revised 4 August 2025; accepted 23 August 2025. Date of publication 10 September 2025; date of current version 25 September 2025. This work was supported in part by Taighde Éireann—Research Ireland and the Department of Agriculture, Food and Marine on behalf of the Government of Ireland, co-funded under the European Regional Development Fund under Grant 21/RC/10303_P2 (VistaMilk); in part by the CONNECT Centre for Future Networks and Communications, co-funded under the European Regional Development Fund under Grant 13/RC/2077; in part by the Insight Centre for Data Analytics, co-funded under the European Regional Development Fund under Grant SFI/12/RC/2289-2 and Grant 16/RC/3918-CONFIRM; and in part by the Enterprise Ireland funded Holistics Disruptive Technologies Innovation Fund (DTIF), co-funded under the European Regional Development Fund under Grant EI-DT20180291-A. *(Corresponding author: Nadeem Rather.)*

Nadeem Rather, Dinesh R. Gawade, John L. Buckley, Brendan O'Flynn, and Salvatore Tedesco are with the Wireless Sensor Network Group, Tyndall National Institute, University College Cork, Cork, T12 K8AF Ireland (e-mail: nadeem.rather@tyndall.ie).

Roy B. V. B. Simorangkir is with the Department of Engineering, Durham University, DH1 3LE Durham, U.K.

Digital Object Identifier 10.1109/JRFID.2025.3608617

I. Introduction

Chipless RFID (CRFID) technology has been shown to have significant potential for use in emerging real-world IoT applications such as wireless identifications, health monitoring, tracking, and sensing, to name a few [1], [2].

In the literature, the most common approach used to realize frequency domain based CRFID tags is by using radar cross section (RCS) methods [2]. The RCS of the tag is utilized to extract tag information using backscattered electromagnetic (EM) waves, which are interrogated from the reader antenna. The CRFID tag's RCS depends on the incident wave's polarization, the angles of incidence and observation, the tag's geometric configuration, its electrical characteristics, and the operational frequency [3]. Moreover, based on the geometry of the tag and the polarization of the incident and reflected waves, RCS-based CRFID tags can further be categorized into co-polarization (co-polar) and cross-polarization (cross-polar) based tags. The co-polar tags are designed to keep the incident and reflected wave polarization in the same polarization. While for cross-polar tags, the incident and reflected waves are orthogonally polarized. The cross-polar CRFID tags, also known as depolarizing tags, can modify the polarization of the incoming wave upon reflection based on the resonator geometry [4]. This requires the readers' transmitting and receiving antennas to be oriented perpendicularly to each other in a cross-polar configuration, as shown in Fig. 1.

The cross-polar class of tags are developed to mitigate challenges in applying CRFID tags in real-world settings, where the tag's response is influenced by background reflections [5], [6], [7], [8], [9], [10]. Reflections from objects placed behind the tag significantly affect the co-polar RCS, making the identification of co-polar tags more challenging. Since most of the objects in the environment reflect radar signals with the same polarization as they receive (co-polar RCS), using cross-polar CRFID tags offers new potential advantages by minimizing the impact of environmental reflection effects in the tag's response, thereby enhancing detection range and accuracy (shown in Fig. 1) [7], [9], [11]. Unlike polarization-independent tags, which address orientation insensitivity, depolarizing tags tackle background environmental reflection suppression [12].

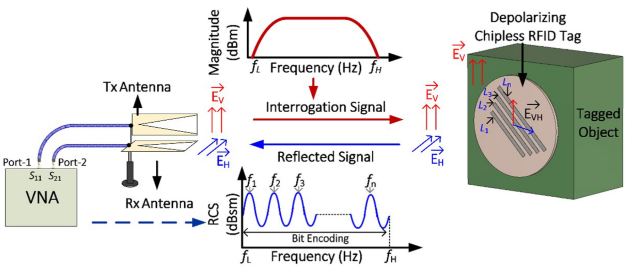

Fig. 1. An overview of a depolarizing Chipless RFID System.

This makes them particularly valuable when CRFID tags are applied to lossy, reflective, or cluttered surfaces where co-polar interference is significant [4], [13], [14]. Several resonator topologies have been developed in the literature to achieve a depolarizing response from the tags. For example, in [6], the authors developed a depolarizing CRFID tag design for an on-human body application. The tag is developed using six L-shaped resonators to achieve the cross-polar component. A ground plane is added behind the tag's substrate to mitigate the RCS sensitivity to the proximity of a human body. Furthermore, it is also utilized to enhance the quality factor of the resonators. The unique L-shape of each resonator induces currents in two orientations, vertical and horizontal, which, when excited by a vertically polarized plane wave, result in reradiated fields with both vertical and horizontal components. Furthermore, the authors also show that an array of 45° slanted dipoles can be utilized to achieve cross-polar response from the tags.

In [7], the authors utilized various resonator shapes, such as spiral, slanted dipole strips, leaf shape, hairpin, and flower shape resonators, to achieve depolarizing tags. In [8], a 45° slanted dipole strip and a vertical dipole strip were used to achieve robust detection due to the utilization of both co-polar and cross-polar components of the tag response. The cross-polar signal strength is approximately 25–30 dB lower than that in co-polarization implementations [13]. This reduction in RCS necessitates more effective data processing methods considering various physical parameters, including tag bending effects, varying read ranges, and differing electrical permittivity of the objects to which the tags are attached. This paper reports for the first time an end-to-end deep learning (DL) workflow for robust detection of depolarizing chipless RFID tags. Building on the research described in [12], where a first-of-its kind ML-assisted robust detection method was developed for the co-polar class of tags on varying surface shapes, orientations, and read ranges.

In this paper, an additional aspect of platform material properties was further investigated for robust signal detection for depolarizing CRFID tags. Additionally, part of the novelty in this work is in the fact that a unique advanced hybrid neural network architecture was employed that incorporates Bidirectional Long Short-Term Memory (Bi-LSTM) layers and convolutional layers (CNN) to enhance detection precision. Furthermore, these models were augmented with attention mechanism layers, providing valuable insights into the models' performance and operations using data visualization techniques, which has not been reported previously for this domain.

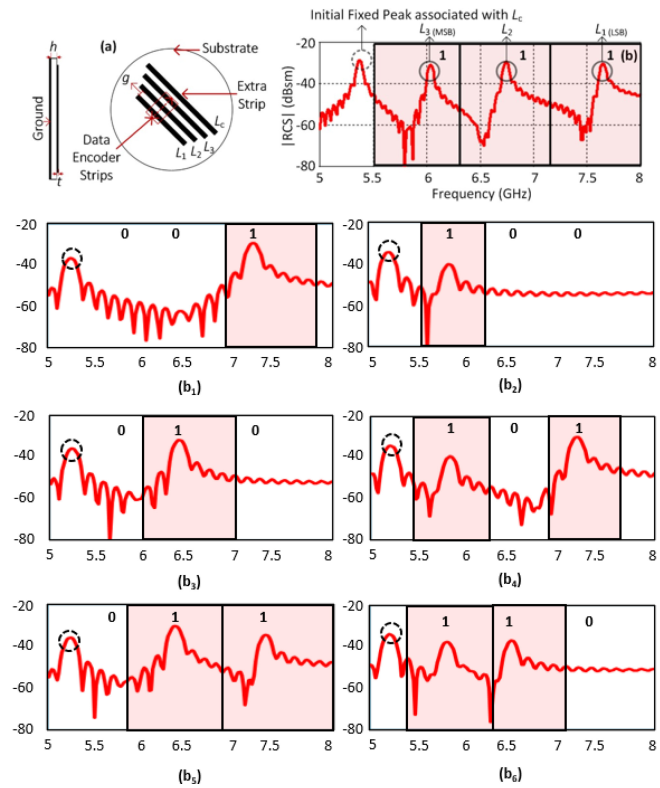

Fig. 2. (a) Geometry of the proof of concept: tag I ('111'). Dimensions (all in millimeters) are: L_1 = 14, L_2 = 16, L_3 = 18, L_C = 20, width of dipole elements = g = 1, h = 0.79, and t = 0.035. (b) EM simulated Depolarized RCS response of the Tag (Tag ID 7), (b_1) = ID 1, (b_2) = ID 2, (b_3) = ID 3, (b_4) = ID 4, (b_5) = ID 5, (b_6) = ID 6.

II. 3-Bit Depolarizing CRFID Tag

For this study, a 3-bit depolarizing chipless RFID tag was developed using 45° slanted dipoles based on [7], [13] (shown in Fig. 2 (a)). A first-of-its-kind method was however introduced to enhance data detection using an additional dipole element (L_c). The extra dipole strip in this study was utilized to create a fixed peak in the RCS response similar to the outermost ring discussed in [15]. However, the functionality of this new design was to improve the deep learning accuracy by introducing a fixed peak or a reference in all the signal variations. The dipole elements (all dimensions provided in the caption of Fig. 2) were fabricated on a thin circular grounded Rogers 5880 substrate (ϵ_r = 2.2, $tan\delta$ = 0.0009 at 6.5 GHz) with 0.79 mm thickness. The fabrication was carried out using an LPKF ProtoMat S104 PCB circuit board plotter with a fixed substrate diameter of 25 mm for each tag [16]. The tag design was investigated through EM simulations conducted in CST Microwave Studio 2022 [17]. The tag was excited using vertically polarized plane waves, and an RCS probe was utilised to calculate the tag's cross-polar RCS.

The EM-simulated cross-polar RCS response was utilized to validate the encoding principle of the proposed design methodology. As shown in Fig. 2 (b), the response from each dipole element created a peak in the cross-polar RCS response. The first peak is due to L_c dipole element and is kept fixed for this study, while the remaining three peaks (due to the encoding dipole strips L_1, L_2, L_3) are utilized for 3-bit binary encoding (ID 1 – 7). The dipole 'L_3' represents the most significant bit (MSB), and 'L_1' represents the least significant bit (LSB). The presence of the dipole element and its peak is utilized to represent binary logic-1, while the absence of the dipole element and its associated peak are utilized for representing binary logic-0. While the slanted dipole concept is adapted from previous works [7], [13], [18], the inclusion of a fixed reference dipole (L_c) to produce a baseline RCS peak for deep learning model calibration is novel to uniquely enhance model alignment and detection consistency.

Each tag ID was independently fabricated by selectively omitting the relevant encoding dipoles during layout design, rather than through physical removal after fabrication. A frequency range of 5 to 8 GHz was utilized within the UWB band of 3.1 to 10.6 GHz to encode the binary data. The 3-bit encoding was selected to validate detection robustness using developed DL models, under tag deformation, read ranges, orientation, and material variability. The utilized frequency band falls within the UWB RFID spectrum, suitable for applications such as short-range sensing, healthcare monitoring, and logistics [2].

A. Experimental Characterization

In order to measure these tags, a two-antenna bistatic RCS measurement approach was chosen to measure the cross-polar RCS response of the fabricated tags. As shown in Fig. 3(a), the measurement setup consisted of two linearly polarized wideband Vivaldi antennas. The fabricated tapered slot Vivaldi antenna were utilized as the reader antenna for both transmission and reception. The antenna dimensions are 90 mm × 53 mm, featuring a tapered exponential slotline with a microstrip feed and balun transition. Its measured S_{11} response exhibits a wideband performance from approximately 4.5 to 8.5 GHz. The Vivaldi antenna was selected because of its directive radiation pattern, stable gain, and linear polarization, making it well suited for bistatic depolarized RCS-based measurements with reduced multipath interference.

Experiments were conducted in a controlled laboratory environment, isolated from external personnel interference. The tags being tested were mounted on a support structure positioned 50 mm away from both the transmitting and receiving Vivaldi antennas. The transmitting and receiving antennas were set perpendicular to each other to measure the cross-polarized response of the tags. The two antennas were connected to a two-port Anritsu MS2038C Vector Network Analyzer (VNA) [19]. In practical RFID setups, depolarized tag responses are captured via a cross-polar configuration with orthogonally polarized reader antennas. The receiving antenna detects only the signal components that are cross-polarized relative to the transmitted wave, allowing cleaner isolation of the tag's response. The transmitting Vivaldi antenna was connected to port-1 of the VNA and was oriented vertically to interrogate the tag using a vertically polarized plane wave.

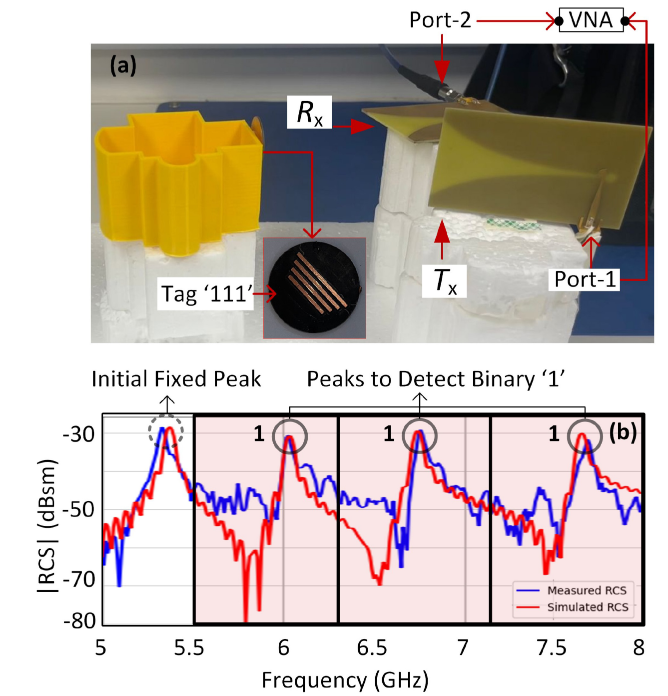

Fig. 3. (a) Bistatic cross-polar RCS measurement setup, (b) Simulated (in Red) vs Measured (In Blue) RCS response.

Port-2 of the VNA was connected to a horizontally orientated Vivaldi antenna and was utilized as the receiving antenna to receive the depolarized, horizontally polarized reflected waves from the tag. A continuous 5 to 8 GHz signal at 0 dBm RF power was generated at port-1 using the VNA, and the transmission coefficient (S_{21}) was measured at port-2. The cross-polar RCS was determined using the method described in [13] and using equation (1).

$$\mathrm{RCS}(\sigma) = \left|\left(S_{21_{\mathrm{Tag}}} - S_{21_{\mathrm{Iso}}}\right)\right|^2 \mathrm{m}^2 \tag{1}$$

This expression adapted from [13], is utilized when the objective includes tag ID detection based on resonance features, therefore, not requiring calibration with a reference object. However, calibration is required for applications that rely on precise amplitude or phase measurements.

Similarly, in Fig. 3(b), the simulated and measured cross-polar RCS response of the developed tag-I with encoded ID '111' is shown, indicating the successful implementation of the tag synthesis process.

III. Experimental Framework and Data Collection Approach

In this study, data was acquired using the setup illustrated in Fig. 4 [20]. To implement deep learning models that incorporate all possible scenarios in the training dataset, a total of 21 tags were fabricated.

To preserve measurement integrity and repeatability, 21 tags were fabricated in advance rather than reusing or altering a single tag. These tags consisted of 3 sets of 7 tags, each set consisting of Tag ID 1-7 (001, 010, 011, 100, 101, 110, and 111). The fabricated tags were then used for data

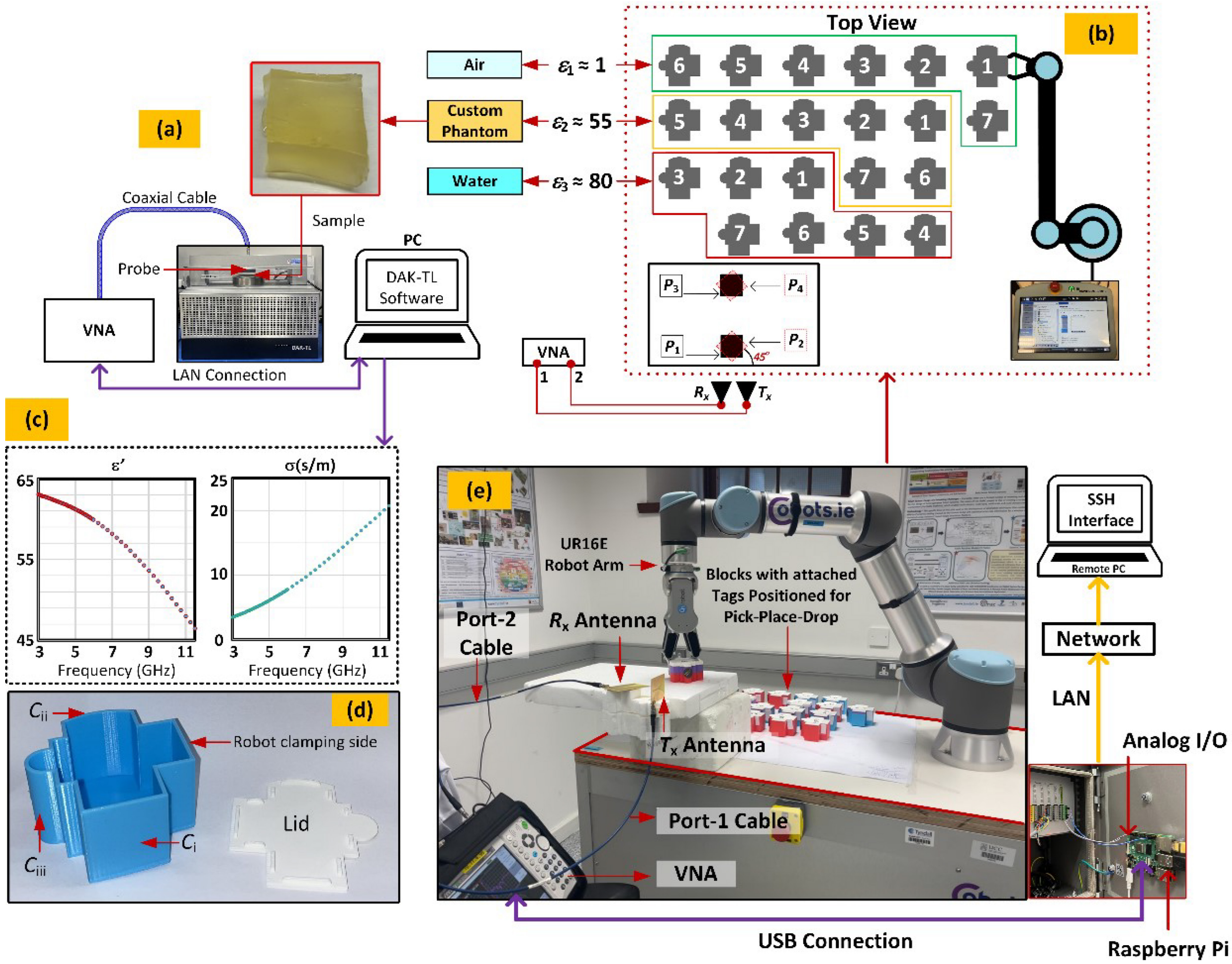

Fig. 4. Overview of the developed Automated Data Acquisition System: (a) Developed muscle-mimicking phantom validated using a dielectric assessment kit, (b) Top view illustrating the distribution of 21 blocks used for pick and place, (c) Dielectric properties of the phantom designed to mimic a medium permittivity case, (d) 3D printed blocks with a lid created to mimic various shapes and accommodate different muscle and water phantom gels. (e) The UR16e robot-based measurement setup interfaced with the VNA.

collection. To capture the cross-polar RCS of the tags, the measurement setup depicted in Fig. 4(e) was employed. This setup included an Anritsu MS2038C Vector Network Analyzer (VNA) interfaced with a Raspberry Pi (RPi) via a Secure Shell (SSH) connection, with Python used for programming. Automation, communication, and RCS calculations were facilitated by libraries such as PyVISA, NumPy, and Pandas.

A vertically oriented transmitting Vivaldi antenna was connected to port-1 of the VNA to emit EM waves toward the tag, while a horizontally oriented receiving Vivaldi antenna was connected to port-2 to receive them. The VNA performed a frequency sweep from 5 to 8 GHz with an RF output power of 0 dBm, and the transmission coefficient (S_{21}) was recorded at Port-2. To introduce variations in the physical scenarios for the tag within the dataset, 21 hollow 3D-printed structures were used.

These structures were printed using RS PRO 1.75 mm Polylactic Acid (PLA) filament, with dielectric properties (ϵ_r = 2.7, $tan\delta$ = 0.0009 at 2.45 GHz [21]), as illustrated in Fig. 4(d).

For each tag ID, the measured data was collected for the following cases:

- Mounting Platforms for Physical Deformation: The tags were affixed to three distinct mounting platforms to mimic the physical deformation of the tag. This was enabled by utilizing three sides of the 3D-printed structure, encompassing a planar side to mimic a planar case-i (C_i) and two cylindrical sides to mimic cylindrical tag bends of 40 mm case-ii (C_{ii}) and 10 mm case-iii (C_{iii}), as shown in Fig. 4(c).
- Surface Material Properties: The tag was affixed to the blocks with three varying material properties. This was enabled by filling the hollow 3D blocks with materials having an electrical permittivity of low ($\epsilon_1 \approx 1$), medium ($\epsilon_2 \approx 55$), and high ($\epsilon_3 \approx 80$) values. For this study, air and water were used to mimic the low and high permittivity values. Moreover, a plant-based gelatin agar was mixed with water to convert it into a gel, avoiding any spillage during the measurements. As given in [22], agar does not significantly vary the

dielectric properties of the water. Furthermore, a human muscle mimicking phantom was developed to prepare the medium case using the recipe given in [23]. The following ingredients were combined by weight in units of grams to develop the broadband muscle tissue-mimicking phantom: Water (230), Gelatine (34.1), NaCL (1.4), Oil (75), and Detergent (40). As shown in Fig. 4(b), the dielectric material properties of the prepared phantom were measured and validated by a dielectric assessment kit, DAK-TL-3.5 from SPEAG [24]. The results were in good agreement with the measured dielectric properties given in [23], with an average measured electrical permittivity (ϵ_1) of = 55, as shown in Fig. 4(c).

- Read Range and Orientation: To incorporate varying signal-to-noise ratios in the measurements, two read range variations were incorporated at position P_1 and P_3 at 50 mm and 150 mm, respectively. Furthermore, at P_1 and P_3, a 45° orientation shift was included, represented by positions P_2 and P_4, as depicted in Fig. 4(b).

The process of picking and placing the blocks, attached with tags, was automated using the Universal Robot (UR16e), featuring 6 rotating joints, a movement speed range of 120-180 degrees per second, and a repeatability tolerance of ± 0.05 mm [25]. Communication between the robot and the VNA was facilitated via the Raspberry Pi. For each mounting platform condition (*Ci* - *Ciii*), the 3D blocks were arranged in three groups, with each group containing Tags with ID 1-7, as depicted in Fig. 4(b). The robot started from a rest/wait position, and an initial measurement with all structures in place, except the tag, was conducted to capture isolation reflections (S_{21Iso}). After that, a predefined movement signal was sent to the robot to pick, place, record (S_{21Tag}), and replace the structures individually for all 21 tags.

After completing measurements for case-I (*Ci*), tags were manually repositioned to different sides of the structure for cases *Cii* and *Ciii*, and the process was repeated. To account for noise variations and interference, 50 readings were taken for each tag measurement scenario. The dataset thus consisted of 12,600 labeled depolarized RCS EM signatures. Each sample was a one-dimensional signal with 700 frequency-domain points (5–8 GHz range), derived from S_{21} measurements converted to RCS using Equation (1). The labels correspond to tag IDs (1–7), determined by the presence or absence of encoded resonator peaks. The dataset incorporates a wide variety of conditions—tag deformations (C_i, C_{ii}, C_{iii}), read ranges (P_1, P_3), and orientations (P_2, P_4), and surface materials with different permittivities (ϵ_1, ϵ_2 and ϵ_3)—to enable generalization under real-world deployment.

The rate of data acquisition was mainly influenced by the Intermediate Frequency Bandwidth (IFBW) setting of the VNA, which was configured to 10 kHz in this case. With these settings, each data sweep took approximately one second to complete.

A. Deep Learning Modelling

After collecting the dataset, a series of pre-processing steps were applied to the raw data to prepare it for implementing the Deep Learning (DL) neural network models.

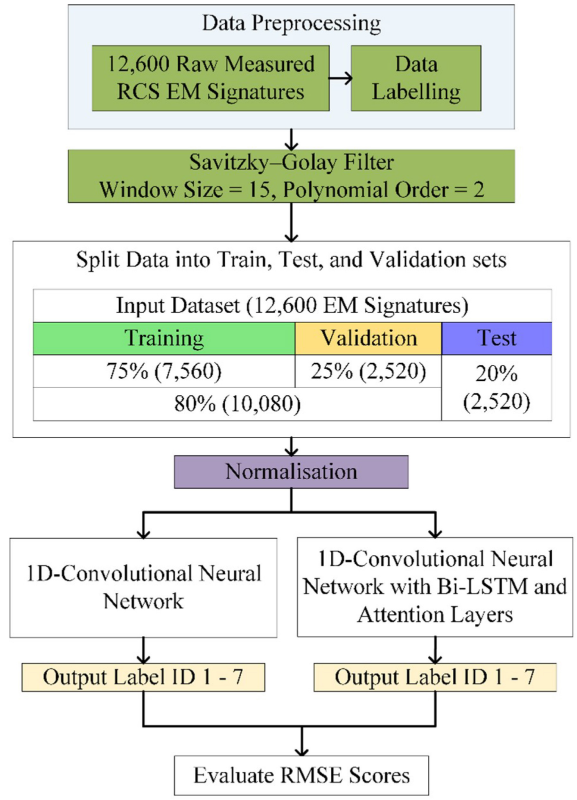

Fig. 5. Basic flow diagram of the overall deep learning process.

The process flow is illustrated in Fig. 5. First, the labeled data went through a smoothing process to reduce unwanted noise from the undesired RF and electrical interferences, such as from the surrounding environments and reader instrument.

The process aimed to reduce the noise while retaining the vital signal elements required for ID detection, such that RCS peaks in the frequency response. In order to implement an efficient smoothing method, a comparative analysis of four different filtering methods (Savitzky-Golay (Savgol), Butterworth, Moving Average, and Median) was conducted to identify the most effective approach that would retain the peak RCS amplitude levels and their respective resonant frequencies without inducing significant distortion.

The Savgol low-pass filter was found to be the most efficient smoothing method for this case [26], [27]. In comparison to Butterworth, Moving average, and Median averaging methods, the Savgol filter minimized the noise while retaining the position of the peaks without altering its amplitude. This is due to the Savgol filter's unique approach of utilizing data points from the entire signal for filtering purposes, in contrast to the other techniques, which are constrained to using only past data points relative to the data point being analyzed.

As shown in Fig. 6, and detailed in Table I, the resulting RCS amplitude levels and frequency positions were compared for Tag ID '111' using all four filtering techniques. As seen, the Savgol filter retained the frequency position of the raw signal with significantly less RCS amplitude distortion.

A Savitzky-Golay filter with a window size of 15 and a polynomial order of 2 was applied to smooth all raw

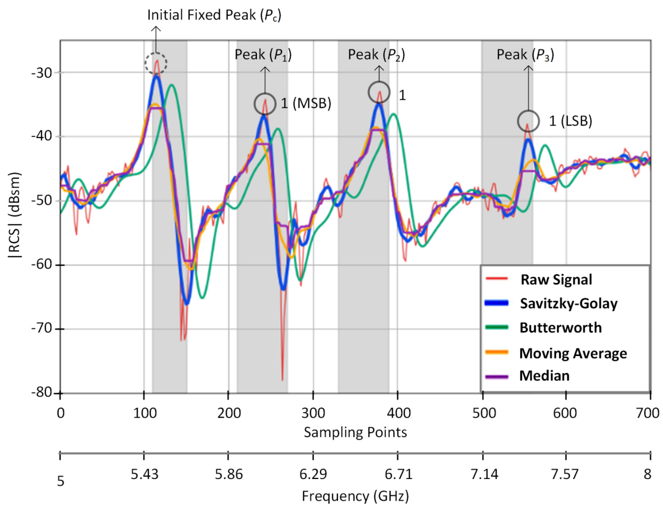

Fig. 6. Comparison of filtering methods on raw RCS data for Tag ID '111', highlighting peak preservation by Savitzky-Golay.

EM signatures. The labeled dataset of 12,600 filtered EM signatures was then consolidated and saved into a single.CSV file. This data was subsequently imported into Python for further processing. Initially, the filtered dataset was divided into training, validation, and test sets, with a stratified approach to maintain a balanced distribution of labels across cases.

The test set comprised 20% of the data, while the remaining 80% was split into training and validation sets with a 75:25 ratio. For normalization, the 'StandardScaler' from the scikit-learn library [28] was applied to the training dataset, with the resulting mean and standard deviation also used to standardize the validation and test sets. This preprocessed data was then employed to train two 1D-Convolutional Neural Network (1D-CNN) models based on regression.

1) Model 1: The architecture of Model-1 featured multiple layers, beginning with the RCS EM signature as the input. For this dataset, the input was structured as 700 data points in a one-dimensional format of (700, 1). This was followed by a Conv1D layer containing 512 filters with a kernel size of 7, designed to capture local patterns within the input data. Next, a MaxPooling1D layer was applied to decrease the spatial dimensions. To mitigate overfitting, a Dropout layer with a rate of 0.5 was incorporated. Further layers included additional Conv1D layers with progressively smaller filter sizes of 256, 128, 64, and 32, each employing a kernel size of 7.

After the Conv1D layers, a MaxPooling1D layer was included to further reduce dimensionality, with dropout layers at a 0.5 rate to minimise overfitting. BatchNormalization layers were strategically placed within the architecture to normalize layer inputs across each batch. Towards the end of the architecture, a Flatten layer was introduced to convert the data into a one-dimensional vector. This flattened vector was then passed through fully connected layers with Rectified Linear Unit (ReLU) activation, comprising a Dense layer with 1,500 units, a Dropout layer set to 0.5, and another Dense layer with 500 units. The final output layer used a Dense layer with a linear activation function to facilitate regression-based prediction of the tag ID.

2) Model 2: The architecture for Model-2 employed a hybrid approach, incorporating Conv1D, Bidirectional Long Short-Term Memory (Bi-LSTM), and attention mechanism layers. This combination leverages the Conv1D layers for capturing local signal patterns, while Bi-LSTM layers handle recurrent memory management, and attention layers apply adaptive attention weights. Hybrid CNN architectures integrate the local feature extraction capabilities of CNN with the sequential modelling advantages of Bi-LSTM layers and the adaptive focus provided by attention mechanisms. While 1D CNNs effectively capture local spatial features—such as RCS peak locations and magnitudes, they are limited in modelling long-range dependencies across the EM spectrum [29], [30]. The incorporation of Bi-LSTM layers addresses this limitation by capturing sequential correlations that may arise from varying tag IDs, physical distortions, and material-induced frequency shifts. Similar hybrid frameworks have demonstrated improved robustness and interpretability in radar signal classification and RF interference analysis [31], [32].

In this case the model began with an input layer, consistent with that of Model-1. The input layer was followed by two Conv1D layers of 256 and 128 filter size, each followed by a MaxPooling1D and a dropout layer for reducing dimensionality and overfitting. Another Conv1D layer with a filter size of 64 was added, followed by a MaxPooling1D layer. The next section of the architecture consisted of the two Bi-LSTM layers. The Bi-LSTM layers introduced a bidirectional flow of information through the network. Unlike the traditional LSTM layers that capture temporal dependencies in only one direction, Bi-LSTM layers process sequences bi-directionally to effectively capture information from past and future time samples, enhancing their ability to understand complex patterns in sequential data. Furthermore, an attention layer was added to introduce a dynamic weighting mechanism to the outputs of the Bidirectional LSTM layers. Instead of utilizing all the samples of the input sequence equally, the attention layer uses a mechanism to assign varying levels of importance to different parts of the sequence based on their relevance.

This allows the model to focus on relevant features, improving its performance in capturing local patterns in the data [33]. Both models were trained using the Adam optimizer [34] and the mean squared error (MSE) as the loss function. The training process used a batch size of 32 and ran for 300 epochs. To optimise the process, early stopping was applied to monitor the training loss and halt training if there was no improvement over a specified number of epochs. Training loss was tracked to assess model convergence and performance, and model checkpoints were employed to save the best-performing model. Model performance was evaluated with root mean square error (RMSE), an evaluation metric that indicates the average difference between predicted and actual values, expressed in the same units as the target variable. The models were initially trained on the training set and subsequently validated to ensure no overfitting. Once confirmed, the architectures were further trained on the development set and finally tested on the independent test dataset.

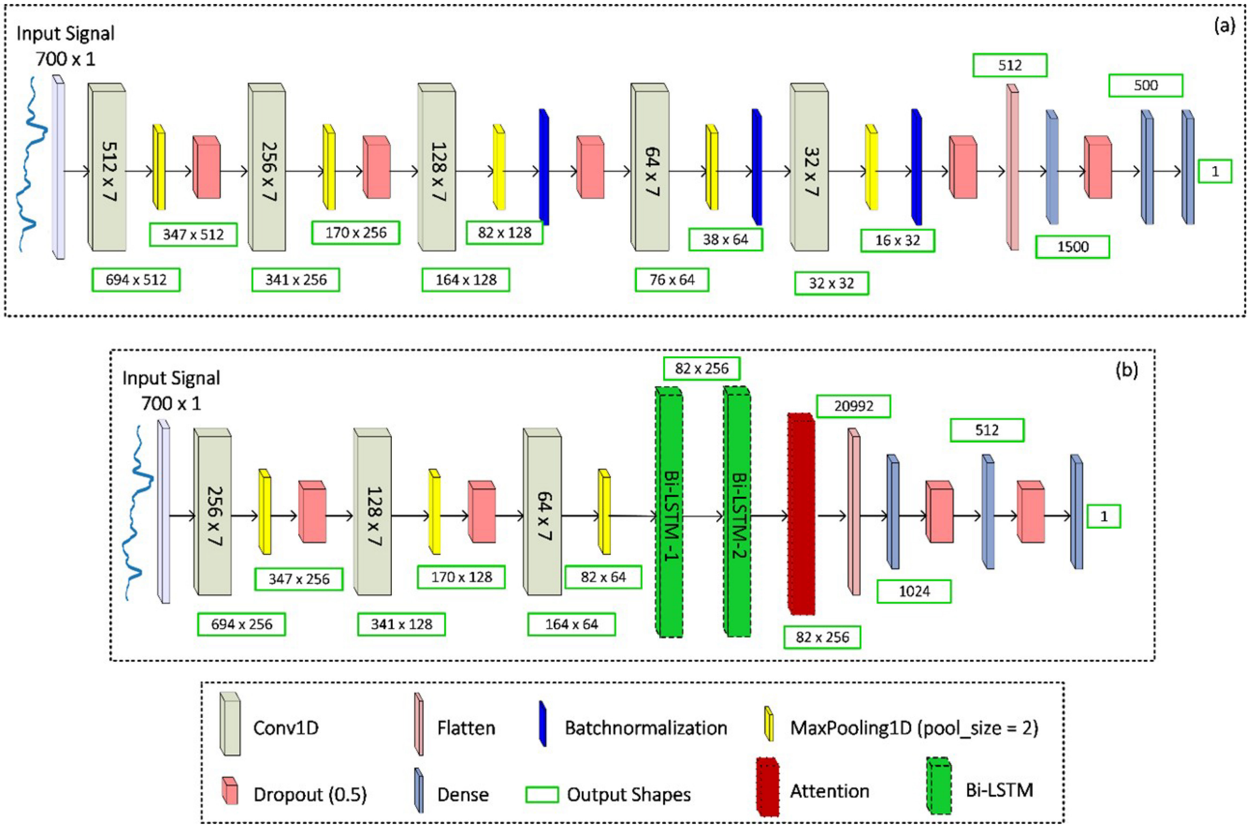

Fig. 7. Developed deep learning models. (a) Model-1 based on 1D-CNN. (b) Model-2 using 1D-CNN with Bi-LSTM and attention mechanism.

TABLE I
COMPARISON OF RCS PEAK VALUE AND POSITION FOR DIFFERENT FILTERING TECHNIQUES

Name	P_C (dBsm)	P_C (GHz)	P_1 (dBsm)	P_1 (GHz)	P_2 (dBsm)	P_2 (GHz)	P_3 (dBsm)	P_3 (GHz)
Raw Signal	-28	5.49	-34	6.03	-33	6.62	-38	7.37
Savitzky-Golay	-30.5	5.49	-36.1	6.03	-34.7	6.62	-40.5	7.37
Butterworth	-32	5.52	-38.8	6.08	-36.1	6.67	-41.2	7.42
Moving Average	-35	5.49	-40.5	6.02	-38.2	6.61	-43.5	7.38
Median	-35.2	5.49	-41.1	6.03	-39	6.62	-45	7.37

IV. RESULTS

Table II presents the RMSE results for the two deep learning models, detailing their performance across the training, validation, and test sets. Both models demonstrated strong generalisation, accurately predicting on previously unseen data. Model-1 achieved a notable performance, with a low test set RMSE of 0.040 and a relative error of 0.66%. However, Model-2 using the hybrid approach reduced the error further by 27.5%, with a RMSE of 0.029 (0.48%) on the unseen test dataset. These results showcase the potential of using a hybrid technique to achieve accurate predictions in this domain. For Model-2, a technique to visualize the attention mechanism was also carried out. This was enabled by using the best-performing Model-2 architecture.

One of the advantages of using visualization techniques is to "see" where the model is looking in the EM signature when making predictions. The attention mechanism, drawing inspiration from the human visual system's ability to focus selectively on certain regions, significantly enhances the performance and accuracy of deep learning models.

TABLE II
SUMMARY OF RMSE RESULTS FROM MODEL-1 AND MODEL-2

DL Model	Train	Validation	Test
Model-1	0.064	0.073	0.040 (0.66%)
Model-2	0.028	0.032	0.029 (0.48%)

This mechanism functions by computing a score or weight for each pair of input and output elements, aggregating the input features into a context vector that is instrumental in generating the output element or next hidden state [35].

By visualizing these attention weights, typically through heatmaps, the model's decision-making process can be observed to see which parts of the input data are considered most relevant for predictions by the model. For this, a random set of seven EM signatures encoding Tag ID 1–7 from the unseen test signal were utilized for visualization (as shown in

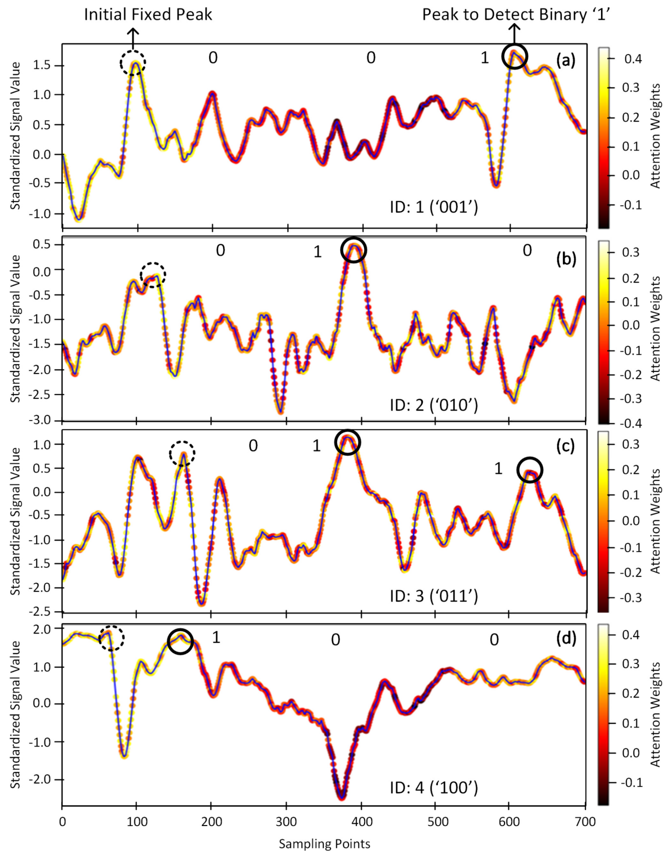

Fig. 8. Visualization of attention weights for (a) Tag ID 1 ('001'), (b) Tag ID 2 ('010'), (c) Tag ID 3 ('011'), (d) Tag ID 4 ('100').

TABLE III
ACTUAL VS PREDICTED TAG ID USING MODEL-2

Actual ID / C_{i-iii} / ϵ_{1-3} / P_{1-4}	**Predicted ID (Error)**	**Cross-Reference Figure**
1 /C_i / ϵ_1 / P_1	1.06 (+0.06)	Fig. 8 (a)
2 /C_{ii} / ϵ_1 / P_4	2 (0)	Fig. 8 (b)
3 /C_i / ϵ_2 / P_3	3 (0)	Fig. 8 (c)
4 /C_{iii} / ϵ_3 / P_2	4.06 (+0.06)	Fig. 8 (d)
5 /C_i / ϵ_2 / P_1	4.93 (-0.07)	Fig. 9 (a)
6 /C_{iii} / ϵ_2 / P_1	6.07 (+0.07)	Fig. 9 (b)
7 /C_{ii} / ϵ_3 / P_3	7.03 (+0.03)	Fig. 9 (c)
Avg. Error = 0.021		

Fig. 8 and 9). The actual and predicted values are given in Table III. It was also observed that rounding the predicted ID to the nearest whole number reduced the average error from 0.0214 to 0. To enable this functionality, first, the attention weights were extracted from the model.

To ensure a proper correspondence between attention weights and the sequential aspects of the input signal, the attention weights were isolated and resized to align with the length of the original input signal (700 samples). The subsequent visual representation was carried out using the Matplotlib library to plot the attention weights overlaid on the test EM signature.

The original EM signature was plotted as a continuous blue line, while overlaying markers were utilized to depict attention weights. The heat map, applied to these markers, showed the magnitude of attention assigned to different segments of the EM signature. The higher attention weights indicated regions considered by the model as of high importance in the EM signature, which were utilized for the ID prediction, according to the attention mechanism. As shown in Fig. 8 and 9, the attention of the model was seen to be consistent for the fixed initial peak in all cases. The attention to this peak supports the hypothesis of utilizing a reference peak to enhance the training and learning of deep learning architectures in this domain.

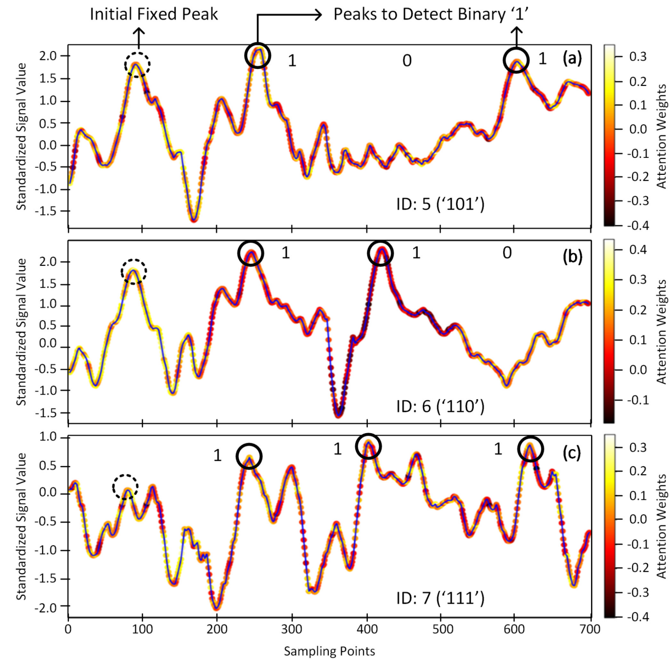

Fig. 9. Visualization of attention weights for (a) Tag ID 5 ('101'), (b) Tag ID 6 ('110'), (c) Tag ID 7 ('111').

Moreover, as shown in Fig. 8 and 9 it was observed that three varying peaks utilized for the 3-bit encoding technique, were prioritized, when differentiating between different EM signatures, further substantiating their importance in the accurate prediction of the ID. This showcased the model's ability to differentiate and leverage the features in the EM signature (RCS peaks) to enhance the prediction rate beyond a singular focus.

In summary, these results showed that the model was learning the correct features from the encoded patterns to make predictions. However, in some complex cases where the predominant features (relevant peaks) were not clear, it was observed that the model distributed attention across the entirety of the input signal. This behaviour was evident in scenarios such as in Fig. 8 (b), where scattered points of attention were observed throughout the signal.

V. DISCUSSION

The experimental results demonstrate that the proposed 3-bit depolarizing CRFID tag, combined with a DL-based detection framework, can achieve reliable tag identification across significant environmental and geometric variations. A key contributor to this robustness is the inclusion of a fixed reference dipole (L_c), which introduces a stable peak in the RCS response and serves as an anchor point for the learning models.

TABLE IV
COMPARISON OF THE PROPOSED WORK AGAINST STATE-OF-THE-ART CHIPLESS RFID TAGS

Ref.	Resonator Shape	Size (mm)	Bits	Freq. (GHz)	Substrate	Pol./ Meas. Method	Surface Type	ML/DL Method	Performance Metric
[6]	L-shaped	85×33	6	3–7.5	Rogers RO4003C	Depolarizing/ Bistatic	On-body	None	Detection Rate: NA
[7]	Slanted Dipoles, Flower	NA	3–8	4–8	Taconic TLX-8	Depolarizing/ Bistatic	Varying surfaces	None	Detection Rate: NA
[36]	Alpha-Numeric	50×10	5	57–64	FR-4	Cross Pol./ Bistatic	Varying surfaces	Subspace KNN, Bagged Trees, Weighted KNN, Fine KNN	Accuracy: 92.6–95.3%
[37]	T-Shape	$\approx 110 \times 45$	2	2–8	PET	Cross Pol./ Bistatic	Varying Lossy Materials	Decision Trees, k-NN, LDA, SVM	Accuracy: 86.9–98.5%
[38]	Octagonal	50 mm^2	5	2–8	FR-4	Co-pol./ Bistatic	Mixed surfaces	SVM, k-NN, Decision Tree, LR, NB	Accuracy: 93.47%
[39]	SRR / CRR Array	120 mm^2	4	2–3.5	FR-4	Co-pol./ Bistatic	Polystyrene Foam	LR, SVM, RF, NN, kNN	Accuracy: 93.3%
This Work	**Slanted Dipole + Ref. Dipole**	**⌀ 25 (circular)**	3	5–8	**Rogers 5880**	**Depolarizing/ Bistatic**	**Varying Lossy and Curved Surfaces**	**1D-CNN + Bi-LSTM + Attention**	**RMSE: 0.040 - 0.029**

Pol. = Polarization, Meas. = Measurement, ML = Machine Learning, DL = Deep Learning, SVM = Support Vector Machine, k-NN = k-Nearest Neighbors, LDA = Linear Discriminant Analysis, PCA = Principal Component Analysis, Reg. = Regression, SRR = Split Ring Resonator, CRR = Complementary Ring Resonator, CNN = Convolutional Neural Networks, NN = Neural Network, LR = Linear Regression, NB = Naive Bayes, Bi-LSTM = Bidirectional Long Short-Term Memory.

This design choice enables more effective feature alignment and consistent attention focusing, particularly under signal distortions caused by material and shape variability, which is a significant advancement for CRFID systems deployed in diverse IoT environments [40], [41].

The comparative performance evaluation between the two models reveals that the hybrid CNN–BiLSTM–Attention architecture significantly outperforms the CNN-only baseline. The hybrid model achieved a 27.5% reduction in RMSE, confirming that temporal sequence modelling and dynamic attention weighting are well-suited for capturing the non-linear variations introduced by real-world tag deployment conditions. The attention weight analysis further verified that the model consistently focuses on relevant regions in the spectrum, particularly near the encoding and reference peaks, validating both the tag design and the model architecture. To further benchmark the effectiveness of the proposed system, Table IV presents a comparative overview of recent state-of-the-art CRFID systems. As observed, only some of the existing designs employed AI methods for the detection of CRFID data, and even fewer combine them with depolarized tags. Unlike prior works that often rely on fixed planar substrates or co-polarized reading setups, the proposed approach demonstrates generalizability across multiple types of surfaces, including lossy and reflective substrates, tags with mechanical deformations, and changes in read orientation. This addresses one of the key challenges in practical CRFID systems, where conventional tags struggle to maintain consistent readability outside controlled environments. Furthermore, the combination of slanted dipole array with a reference dipole, leveraging DL architectures, has not been reported in prior CRFID systems.

Although this study uses a 3-bit tag as a proof-of-concept to validate model robustness under complex variations, the overall tag architecture and learning framework are scalable. Higher-bit encodings can be realized through the inclusion of additional resonators, dual-polarization geometries, or multi-layered substrates, as shown in recent chipless RFID works [42], [43]. These extensions will be explored in future work alongside the integration of passive sensing elements within the tag structure.

Overall, this work presents a combined tag–algorithm solution that enhances CRFID performance through polarization-domain isolation and learning-based interpretation, paving the way for robust deployment in wearable, industrial, and biomedical sensing applications.

VI. CONCLUSION

In this paper, an end-to-end design methodology was demonstrated to develop a robust depolarizing chipless RFID (CRFID) system. In order to enable tag detection on surfaces with RF losses, in the first section, a 3-bit depolarizing CRFID tag based on 45° slanted dipole strips was designed and developed. The novel approach of adding an extra dipole element was introduced to create a reference peak at the beginning of the EM signature, encoding the data, to enable improved data detection performance. Subsequently, three slanted dipole strips were utilized as data encoders such that their presence created a peak at the predetermined frequency in the reflected depolarized EM signature.

The presence or absence of the dipole elements, and hence their associated peaks, were used to encode binary logic-1 or 0 values, respectively. Consequently, the tags were characterized and successfully validated using a bistatic radar measurement setup. Furthermore, a deep learning implementation was developed to enable robust detection of ID data from varying tag environments. To enable this, an automated industry-standard robot-based data acquisition method was utilised with a complete implementation plan for incorporating varying tag deformations, orientations, tag surface material properties, and read ranges. Two deep learning models, namely a 1D CNN Model-1 and a hybrid Model-2 incorporating 1D CNN with Bi-LSTM and the attention mechanism were used. The models were evaluated using training, validation and test results, showing strong generalisation capabilities.

Model-1 achieved a low RMSE of 0.040 (0.66%), while the hybrid model further reduced the error by 27.5%, achieving a test RMSE of 0.029 (0.48%). This paper introduces advancements that pave the way for diverse applications, such as on-body CRFID tags for monitoring and tracking, with potential benefits across sectors such as healthcare, logistics, and agriculture.

References

[1] S. K. Behera, "Chipless RFID sensors for wearable applications: A review," *IEEE Sensors J.*, vol. 22, no. 2, pp. 1105–1120, Jan. 2022.

[2] A. Subrahmannian and S. K. Behera, "Chipless RFID: A unique technology for mankind," *IEEE J. Radio Freq. Identif.*, vol. 6, pp. 151–163, Jan. 2022.

[3] N. C. Karmaker, "Tag, you're it radar cross section of chipless RFID tags," *IEEE Microw. Mag.*, vol. 17, no. 7, pp. 64–74, Jul. 2016.

[4] E. Perret, *Radio Frequency Identification and Sensors: From RFID to Chipless RFID*. Hoboken, NJ, USA: Wiley, 2014.

[5] Z. Ali, O. Rance, N. Barbot, and E. Perret, "Depolarizing chipless RFID tag made orientation insensitive by using ground plane interaction," *IEEE Trans. Antennas Propag.*, vol. 70, no. 7, pp. 5235–5245, Jul. 2022.

[6] T. Andriamiharivolamena, A. Vena, E. Perret, P. Lemaitre-Auger, and S. Tedjini, "Chipless identification applied to human body," in *Proc. IEEE RFID Technol. Appl. Conf. (RFID-TA)*, 2014, pp. 241–245.

[7] F. Babaeian and N. C. Karmakar, "Development of cross-polar orientation-insensitive chipless RFID tags," *IEEE Trans. Antennas Propag.*, vol. 68, no. 7, pp. 5159–5170, Jul. 2020.

[8] M. Borgese, F. Costa, S. Genovesi, and G. Manara, "Depolarizing chipless tags with polarization insensitive capabilities," *Electronics*, vol. 10, no. 4, p. 478, 2021.

[9] A. Ramos, Z. Ali, A. Vena, M. Garbati, and E. Perret, "Single-layer, flexible, and depolarizing chipless RFID tags," *IEEE Access*, vol. 8, pp. 72929–72941, 2020.

[10] A. M. J. Marindra, R. Sutthaweekul, and G. Y. Tian, "Depolarizing chipless RFID sensor tag for characterization of metal cracks based on dual resonance features," in *Proc. 10th Int. Conf. Inf. Technol. Elect. Eng. (ICITEE)*, 2018, pp. 73–78.

[11] F. Requena, N. Barbot, D. Kaddour, and E. Perret, "Robustness improvement for chipless RFID reading using Polarization separation," *IEEE Trans. Microw. Theory Tech.*, vol. 71, no. 7, pp. 3173–3188, Jul. 2023.

[12] N. Rather, R. B. V. B. Simorangkir, J. L. Buckley, B. O'Flynn, and S. Tedesco, "Deep-learning-assisted robust detection techniques for a chipless RFID sensor tag," *IEEE Trans. Instrum. Meas.*, vol. 73, pp. 1–10, 2024.

[13] A. Vena, E. Perret, and S. Tedjni, "A depolarizing chipless RFID tag for robust detection and its FCC compliant UWB reading system," *IEEE Trans. Microw. Theory Tech.*, vol. 61, no. 8, pp. 2982–2994, Aug. 2013.

[14] A. Ramos, E. Perret, O. Rance, S. Tedjini, A. Lázaro, and D. Girbau, "Temporal separation detection for chipless depolarizing frequency-coded RFID," *IEEE Trans. Microw. Theory Techn.*, vol. 64, no. 7, pp. 2326–2337, Jul. 2016.

[15] N. Rather, J. L. Buckley, B. O'Flynn, M. Pigeon, and R. B. Simorangkir, "A design methodology for sensing-ready concentric rings-based Chipless RFID tags with effective spectrum use and high coding capacity," *IEEE J. Radio Freq. Identif.*, vol. 8, pp. 1–9, Jan. 2024.

[16] (LPKF Laser Electron. Co., Garbsen, Germany). *LPKF ProtoMat S104 Circuit Board Plotter for the RF and Microwave Range*. (2024). [Online]. Available: https://www.lpkf.com/en/industries-technologies/research-in-house-pcb-prototyping/products/lpkf-protomat-s104

[17] "CST studio suite electromagnetic field simulation software." 2021. [Online]. Available: https://www.3ds.com/products-services/simulia/products/cst-studio-suite/

[18] F. Costa et al., "A depolarizing chipless RF label for dielectric permittivity sensing," *IEEE Microw. Wireless Compon. Lett.*, vol. 28, no. 5, pp. 371–373, May 2018.

[19] (Anritsu, Atsugi, Japan). *VNA Master + Spectrum Analyzer*. (2021). [Online]. Available: https://www.anritsu.com/en-US/test-measurement/products/ms2038c

[20] N. Rather et al., "A novel robot based data acquisition methodology for chipless RFID systems," in *Proc. IEEE 13th Int. Conf. RFID Technol. Appl. (RFID-TA)*, 2023, pp. 49–52.

[21] R. Proesmans, K. Deprez, M. Velghe, and A. Thielens, "An on-body antenna for control of a wireless prosthesis in the 2.45 GHz industrial scientific and medical frequency band," *IET Microw., Antennas Propagat.*, vol. 16, no. 15, pp. 919–932, 2022.

[22] B. Roebuck and S. Goldblith, "Dielectric properties at microwave frequencies of agar gels. similarity to the dielectric properties of water," *J. Food Sci.*, vol. 40, no. 5, pp. 899–902, 1975.

[23] T. Yilmaz, R. Foster, and Y. Hao, "Broadband tissue mimicking phantoms and a patch resonator for evaluating noninvasive monitoring of blood glucose levels," *IEEE Trans. Antennas Propagat.*, vol. 62, no. 6, pp. 3064–3075, Jun. 2014.

[24] (SPEAG, Zürich, Switzerland). *DAK—Dielectric Assessment Kit*. (2024). [Online]. Available: https://speag.swiss/products/dak/overview/

[25] "UR16e heavy-duty, compact cobot." 2024. [Online]. Available: https://universal-robots.com/products/ur16-robot/

[26] R. W. Schafer, "What is a Savitzky-Golay filter? [Lecture notes]," *IEEE Signal Process. Mag.*, vol. 28, no. 4, pp. 111–117, Jul. 2011.

[27] S. D. Yusuf, F. C. Maduakolam, I. Umar, A. Z. Loko, and L. W. Lumbi, "Comparative analysis of savitzky-golay and butterworth filters for electrocardiogram de-noising using daubechies wavelets," *Asian J. Res. Cardiovasc. Dis.*, vol. 2, no. 1, pp. 15–29, 2020.

[28] "StandardScaler." Scikit Learn. 2024. [Online]. Available: https://scikit-learn.org/stable/modules/generated/sklearn.preprocessing.StandardScaler.html

[29] G. Liu and J. Guo, "Bidirectional LSTM with attention mechanism and convolutional layer for text classification," *Neurocomputing*, vol. 337, pp. 325–338, Apr. 2019.

[30] X. Qi, C. Wu, Y. Shi, H. Qi, K. Duan, and X. Wang, "A convolutional neural network face recognition method based on BILSTM and attention mechanism," *Comput. Intell. Neurosci.*, vol. 2023, no. 1, 2023, Art. no. 2501022.

[31] S. Wei, Q. Qu, X. Zeng, J. Liang, J. Shi, and X. Zhang, "Self-attention Bi-LSTM networks for radar signal modulation recognition," *IEEE Trans. Microw. Theory Tech.*, vol. 69, no. 11, pp. 5160–5172, Nov. 2021.

[32] X. Yang and D. Qiao, "Attention-based bidirectional LSTM network for target tracking," in *Proc. IEEE Int. Conf. Electron. Technol., Commun. Inf. (ICETCI)*, 2021, pp. 151–156.

[33] Z. Niu, G. Zhong, and H. Yu, "A review on the attention mechanism of deep learning," *Neurocomputing*, vol. 452, pp. 48–62, Sep. 2021.

[34] S. Bock, J. Goppold, and M. Weiß, "An improvement of the convergence proof of the ADAM-optimizer," 2018, *arXiv:1804.10587*.

[35] M.-T. Luong, H. Pham, and C. D. Manning, "Effective approaches to attention-based neural machine translation," 2015, *arXiv:1508.04025*.

[36] L. M. Arjomandi, G. Khadka, Z. Xiong, and N. C. Karmakar, "Document verification: A cloud-based computing pattern recognition approach to chipless RFID," *IEEE Access*, vol. 6, pp. 78007–78015, 2018.

[37] S. Jeong, J. Hester, R. Bahr, and M. M. Tentzeris, "A machine learning approach-based chipless RFID system for robust detection in real-world implementations," in *Proc. IEEE MTT-S Int. Microw. Symp. (IMS)*, 2021, pp. 661–664.

[38] A. Thomas, M. M. Sylaja, and J. Kurian, "Refinement of Chipless RFID tags across multiple positions for improved recognition reliability through machine learning techniques," *Prog. Electromagnetics Res. C*, vol. 150, pp. 57–68, Dec. 2024.

[39] F. Villa-Gonzalez, J. J. F. Sokoudjou, O. Pedrosa, D. Valderas, and I. Ochoa, "Analysis of machine learning algorithms for USRP-based smart chipless RFID readers," in *Proc. 17th Eur. Conf. Antennas Propagat. (EuCAP)*, 2023, pp. 1–5.

[40] M. El-Hadidy, A. El-Awamry, A. Fawky, M. Khaliel, and T. Kaiser, "Real-world testbed for multi-tag UWB chipless RFID system based on a novel collision avoidance MAC protocol," *Trans. Emerg. Telecommun. Technol.*, vol. 27, no. 12, pp. 1707–1714, 2016.

[41] M. N. Zahid, Z. Gaofeng, T. Sadiq, H. Rehman, and M. S. Anwar, "A comprehensive study of chipless RFID sensors for healthcare applications," *IEEE Access*, vol. 12, pp. 175647–175665, 2024.

[42] Y. Zhao, S. Genovesi, T. Jiang, G. Manara, and F. Costa, "High-capacity chipless RFID system enabled by machine learning predictive models," *IEEE Internet Things J.*, vol. 12, no. 14, pp. 26514–26522, Jul. 2025.

[43] F.-P. Lai and Y.-S. Chen, "A fully ISM-band chipless RFID tag with hybrid encoding for micro-scale asset identification," *IEEE J. Radio Freq. Identif.*, vol. 9, pp. 542–553, Jul. 2025.

Nadeem Rather (Member, IEEE) received the bachelor's degree in electronics and communication engineering, the master's degree (Research) in communication systems, and the Ph.D. degree, further advancing his expertise in the field. He is a Research Engineer with the Tyndall National Institute, University College Cork, Ireland, where he has been conducting research since 2019. His work focuses on developing advanced AI algorithms and innovative techniques to enhance the performance and efficiency of electromagnetic systems, with a particular emphasis on RFID technologies. Additionally, his research extends to the design of RF antennas for wearable health monitoring applications. His extensive industry and research experience complements his academic background, allowing him to make significant contributions to the field of electromagnetic-based systems. Throughout his doctoral journey, his contributions have been recognized through notable accolades. He was honored with the Postgraduate Publication of the Year Award at Tyndall National Institute in 2020 and 2023. Furthermore, his research paper secured the First Place in the Best Student Research Paper category at the International Workshop on Antenna Technology 2021. Additionally, his research work was acknowledged with the Best Demonstration Award at the VistaMilk Conference 2023, highlighting the practical impact of his innovative solutions.

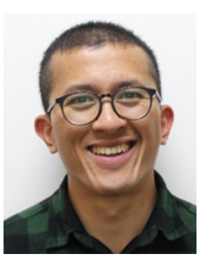

Roy B. V. B. Simorangkir (Member, IEEE) received the B.S. degree in telecommunication engineering from Institut Teknologi Bandung, Indonesia, in 2010, the M.S. degree in electrical and electronic engineering from Yonsei University, South Korea, in 2014, and the Ph.D. degree in electronic engineering from Macquarie University, Australia, in 2018. After completing his Ph.D., he pursued postdoctoral research with Macquarie University; the Institute of Electronics and Telecommunications of Rennes, France; and Tyndall National Institute, Ireland. He is currently an Assistant Professor with the Department of Engineering, Durham University, U.K., where he specializes in the development of unconventional materials-based antennas and sensors for next-generation wireless communication and sensing systems. He has published over 60 refereed research papers in this field, including award-winning work. He has also taken on leadership roles at major international conferences and received recognition as an outstanding reviewer for esteemed journals, notably from 2021 to 2023 for the IEEE TRANSACTIONS ON ANTENNAS AND PROPAGATION.

Dinesh R. Gawade (Graduate Student Member, IEEE) received the Bachelor of Technology degree in electronics and communication technology from the Department of Technology, Shivaji University, Kolhapur, India, in 2016, and the M.Eng.Sc. degree (by Research) from University College Cork, Cork, Ireland, in 2022. He is currently pursuing the Ph.D. degree with Tyndall National Institute and Microelectronic Circuit Center Ireland, Cork. Following his graduation, he gained valuable industry experience as a Hardware Design Engineer from 2016 to 2018. Subsequently, he contributed his expertise to the Indian Institute of Technology Mandi, Mandi, India, as a Project Engineer specializing in Hardware Design. In 2019, he joined Tyndall National Institute, University College Cork, to further advance his research and career. His research interests cover a broad range of topics, including the development of batteryless sensing devices, radio-frequency integrated circuit design, antenna design, low-power sensor node design, and long-range wireless sensor network design for various applications. He was honored with the Wrixon Research Excellence Bursary Award in 2022 for M.Eng.Sc. Research at Tyndall National Institute.

John L. Buckley (Member, IEEE) was born in Cork, Ireland. He received the B.Eng. degree from the Cork Institute of Technology, Ireland, in 1994, and the M.Eng.Sc. and Ph.D. degrees from the Department of Electrical and Electronic Engineering, University College Cork, Ireland, in 2004 and 2016, respectively. From 1994 to 2002, he was with EMC Corporation, Cork, where he specialized in PCB design, high-speed digital design, and signal integrity. He joined the Tyndall National Institute, University College Cork in 2005, where he is currently a Senior Researcher and leads the Antenna and RF Team's research activities working on both fundamental and applied antenna and RF research. He has published more than 80 scientific works and acts as a reviewer for several international antenna journals and conferences in the field of antennas and propagation. His research interests include electrically small antenna design, tunable antennas, wearable and implantable antennas, and RF front-end design. He served as the General Co-Chair for the International Conference on Antenna Technology (iWAT) in 2022.

Brendan O'Flynn (Senior Member, IEEE) received the B.Eng. (Hons.), M.Eng.Sc., and Ph.D. degrees from University College Cork, Ireland. He is currently leading the Human Centric Systems Research cluster in Tyndall and the Head of the Wireless Sensor Networks Group within that research cluster. His research interests include wearable sensing systems, edge-based analytics, sensor system integration, low-power embedded systems design and development, system miniaturization, and RF system design and optimization. He has published widely in these areas and has secured significant funding for the development and deployment of "Smart Sensing" technologies in both fundamental and applied research projects.

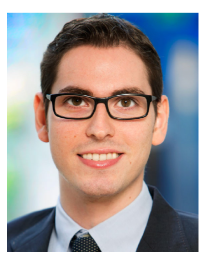

Salvatore Tedesco (Member, IEEE) received the B.Sc. degree (Hons.) in information technology engineering and the M.Sc. degree (Hons.) in telecommunications engineering from the University of Salento, Lecce, Italy, and the Ph.D. degree in electrical and electronic engineering from the University College Cork (UCC), Cork, Ireland. Since April 2012, he has been with the Wireless Sensor Networks Group, Tyndall National Institute, UCC, where he is currently a Senior Researcher and a Team Leader responsible for leading a research team in the wearable and data analytics area. He has authored more than 60 articles in international journals and conference proceedings, and has received over €1.1 million in grant funding as a PI and a Co-PI. Since joining Tyndall, he has managed and successfully led over 20 industrial and research-oriented projects focused on his main research interests on wearable technologies for healthcare and well-being, human motion analysis in sports and clinical populations, digital health, physiological monitoring, signal processing, edge analytics, and machine learning. Further contributions deal with RFID technology and antenna design, ultrawideband localization systems for indoor applications, sensor calibration, and Industry 4.0.